JOURNAL OF GEOPHYSICAL RESEARCH, VOL. 102, NO. D17, PAGES 21,383–21,399, SEPTEMBER 20, 1997

Lagrangian approach for deriving cloud characteristics from satellite observations and its implications to cloud parameterization

E. R. Boer[1] and V. Ramanathan

Center for Clouds, Chemistry and Climate, Scripps Institution of Oceanography
University of California, San Diego

Abstract. A Lagrangian view is adopted for establishing the spatiotemporal cloud statistics and the scale dependent radiative properties using satellite data. Individual clouds are identified using a newly developed scheme. We sort all clouds by cloud type, cloud area, and number of clouds in each area bin, as well as their radiative properties. For seven different cloud types our analyses provide radiative properties, such as albedo and cloud top temperature, as a function of the cloud spatial scale. All clouds are marked by local time, and large clouds are tracked over time. These analyses provide diurnal variability, lifetimes, and evolution of cloud systems as a function of their spatial scales. These scale dependent cloud properties can be objectively used in guiding the development and evaluation of cloud parameterization in global climate models (GCMs). Particularly, we show how our Lagrangian approach can be used to establish the relative importance of resolvable and fully parameterized clouds to the total cloudy area and to the total amount of reflected visible irradiance. Focus in this 1 month satellite study is on the convective-stratiform cloud systems over the western and central tropical Pacific Ocean, including the so-called warm pool. We adopt the hourly Japanese geostationary satellite (GMS) window channel radiances in the visible and IR window region for cloud classification and characterization. To study the radiative contributions of different clouds in the area, we computed the bidirectional model (BDM) for the Visible and Infrared Spin Scan Radiometer instrument aboard GMS, which we show to agree well with the BDM of the Earth Radiation Budget instrument aboard the Nimbus 7 satellite. An iterative two-stage cloud detection scheme was developed to identify individual clouds. Furthermore, a tracking algorithm was developed to study the time evolution of mesoscale convective systems (MCS). It operates on area and orientationally equivalent ellipsoidal representations of these MCS. We show that the temporal statistics of these convective anvil clouds show good agreement with those reported in the literature. Our data indicate that for the convective-stratiform systems in the tropical Pacific, 95% of the radiatively important clouds (containing a core with an effective brightness temperature <219 K) are of scales resolvable by a GCM of about 50 km × 50 km. On the other hand, a GCM of 250 km × 250 km will only be able to resolve 50% of the radiatively important clouds. This, however, does not mean that the processes responsible for the formation and maintenance of these systems are also resolvable. The low clouds that are unattached to convective-stratiform systems are mostly unresolvable by available GCMs.

1. Introduction

Satellite data offer an enormous potential for understanding the spatial and temporal characteristics of clouds. In particular, they offer the only data source for understanding the scale dependence of cloud properties and the lifetimes of cloud systems, two cloud properties which are important for the development and validation of cloud parameterizations in global climate models (GCMs).

Scale dependent cloud properties can only be obtained if individual clouds have been identified. The difficulties involved in defining cloud boundaries using satellite data are akin to clear sky detection with the added complexity that two adjacent clouds may be separated by an optically thin region or by partially cloudy pixels [*Coakley and Bretherton*, 1982]. The process is complicated even more in the case of layered or overlapping clouds decks [*Baum et al.*, 1994]. A step to contribute to this challenging endeavor is presented here.

By organizing the resulting data from individual clouds in terms of cloud type and cloud size we expect this Lagrangian approach to be beneficial in guiding the development and evaluation of cloud parameterization in GCMs, particularly because it may provide insight into which cloud types dominate a particular process at what scales. The basic Lagrangian approach to analyzing satellite data is certainly not novel. It has been used in most studies on mesoscale convective systems (MCS) where these MCS are generally defined by contiguous areas that fall below an effective brightness temperature

[1]Now at Nissan Cambridge Basic Research, Cambridge, Massachusetts.

Copyright 1997 by the American Geophysical Union.

Paper number 97JD00930.
0148-0027/97/97JD-00930$09.00

threshold of around 240 K, often indicating convection or precipitation; see *Mapes and Houze* [1993] for an overview. A similar single-threshold approach is adopted in many cloud-clustering studies [see, e.g., *Lee et al.*, 1994]. Using one temperature threshold bypasses the problem of trying to establish the "true" spatial extent of these systems. Here we propose to use cloud boundaries that are perhaps more closely related to true boundaries such as clear sky or another cloud. Besides using these cloud boundaries in establishing individual clouds we also identify clouds at effective brightness temperatures all the way up to clear sky thereby assigning every cloudy pixel to one particular cloud (section 3.2). We take this extended Lagrangian viewpoint and use it to establish spatio-temporal and radiative cloud statistics.

To discuss the results obtained with our approach in the context of GCMs, it is convenient to differentiate between resolved and subgrid scale clouds. On a technical note, similar to the Nyquist frequency in time series analysis, only clouds whose size exceeds the model's grid scale by a factor of 2 can be considered resolvable. Resolved clouds are defined as clouds whose size exceeds the model's resolution. However, it is important to keep in mind that this does not necessarily mean that the processes leading to the formation and maintenance of these clouds are also resolved. An excellent description of parameterization of resolvable clouds is given by *Sundqvist* [1978]. For these resolved clouds one can use satellite data to validate model simulation of cloud lifetimes and their radiative properties. Subgrid scale clouds are by definition smaller than the spatial scale of the GCM under consideration. Satellite data can be used here to estimate the importance of these subgrid scale clouds to the overall problem.

The above discussion argues for sorting satellite data in terms of the spatial scales, which is one of the major goals of this study. To indicate how our Lagrangian approach can be used to guide GCM cloud parameterizations, we focus on parameterization of cloud-radiative interactions alone and do not consider important issues such as mass and momentum transport of clouds. Since GCM resolution can vary from 50 km $\times$ 50 km to about 500 km $\times$ 500 km, the satellite data have to be organized in terms of scales ranging from a few hundred square kilometers to about 10^6 km^2. As a minimum, we need two quantities: the number of clouds as a function of the area and the radiative properties (narrow albedo and cloud top temperature) as a function of the area. Here we focus on obtaining these two quantities from satellite data. Since we base our analysis on the Japanese geostationary satellite (GMS), we are limited to estimating narrow band albedo and effective radiating temperature. With future improved satellite data, more appropriate variables would include broadband shortwave (SW) and longwave (LW) cloud forcing, cloud height, liquid water path, cloud particle size/phase, and cloud optical depth in the visible or emissivity in the thermal infrared.

Given a GCM resolution, we use the satellite data to estimate two quantities: fraction of the total cloud cover that is due to all of the resolvable scales (i.e., cumulative contribution of all scales larger than the GCM scale) and the cumulative contribution of clouds larger than the GCM scale to the observed albedo. To demonstrate our approach, we use the hourly geostationary satellite data over the western and central tropical Pacific. Even though our approach includes clouds at all scales and at all effective brightness temperatures, we specifically relate our MCS-specific findings to other MCS climatologies in the tropical Pacific [*Mapes and Houze*, 1993; *Mapes*, 1993; *Chen and Houze*, 1996]. To characterize these MCS not only spatially but also temporally, we developed an automated cloud-tracking algorithm (section 3.6). In-depth climatologies and characterizations of MCS in other tropical regions have been described by *Lopez* [1977], *Williams and Houze*, [1987], *Machado et al.* [1992, 1993], *Laing and Fritsch*, [1993], and *Liu et al.* [1995].

2. Data Description

The region of study is the western and central tropical Pacific Ocean between 120°E and 160°W and between 20°S and 20°N. Satellite data were collected hourly between March 7, 1993, and April 7, 1993, during the field phase of the Central Equatorial Pacific Experiment (CEPEX) [*Kuettner*, 1993; *Williams*, 1993]. Data from the Japanese geostationary satellite GMS 4, located on the equator at 140°E, were used in this study. It recorded one full hemispherical disk of visible (0.5–0.75 μm) and infrared (10.5–12.5 μm IR window) radiances every hour. Data for 1300 and 1400 UT were not available because the radiometer was shut off because of the direct Sun beaming into the sensors [*Senta*, 1989]. The nadir visible channel resolution is 1.56 km^2, while the nadir IR window channel resolution is 25 km^2. These data were georeferenced on an equal angle grid with 0.064° longitude and 0.044° latitude resolution (35 km^2 at the equator) using SeaSpace's TerraScan software. The satellite viewing angle, the solar zenith angle, and the relative azimuth angles were retained with the radiometric observations. SeaSpace's standard calibration was performed within the TerraScan software to obtain visible reflectivities and effective brightness temperatures.

The relatively small land bodies in the region of interest rendered land masking the data unnecessary for cloud identification and classification purposes. The clear sky analyses used to establish whether the sensor produced any errors in the effective brightness temperatures were, however, performed on land-masked data, thus producing clear sky effective brightness temperatures representative of open ocean thereby removing the effect of strong diurnal variations over land. Bad scan lines were eliminated by replacing them with the linearly interpolated values of valid surrounding samples. To eliminate the effects of very high Sun zenith angles at the so-called terminator, we did not include pixels whose zenith angle exceeded 80° in our albedo statistics calculations. Furthermore, to avoid any limb-darkening effects, only pixels west of 160°W were used.

The cloud systems in this region are predominantly of convective origin. Deep convective systems in this region lead to extensive stratiform cirrus clouds. Plate 1 shows noontime satellite images with pseudo colored effective brightness temperatures to indicate the extent to which convection, as indicated in black, dominated large portions of this region.

3. Methodology

The method we adopt for analyzing the satellite data consists of six closely related stages: classifying clear sky, identifying individual clouds, classifying clouds by the IR minimum brightness temperature, binning clouds by their size, determining diurnal statistics, and tracking the time evolution of mesoscale convective systems. These steps are described in sections 3.1–3.6. We define T as the satellite-observed effective brightness

temperature and a_{nb} as the narrow band albedo, which is calculated from the observed reflectivities and the derived GMS bidirectional model (BDM) (Appendix A).

3.1. Cloudy and Clear Sky Classification

The necessary first step in cloud identification is to identify clear regions. By definition all other scenes are cloudy. Our basic clear sky classification scheme simply called pixels clear if their T was warmer than 285 K (see dark red regions in Plate 1 for an example case). The threshold T of 285 K was obtained by employing a variant of the spatial coherence technique of *Coakley and Bretherton* [1982]. For each pixel we estimated the mean T of nine pixels (which includes the eight surrounding pixels) and the standard deviation σ. A plot of the mean T against the σ revealed multiple clusters of near-zero σ values (<0.5 K). Pixels with near-zero σ values stem from homogeneous regions in the scene. The mode value of T for each of these clusters revealed clear sky (largest T) and overcast cloud decks (lower values of T). The peak frequency of clear sky occurred around 290 K, and the overcast clusters all occurred at T values colder than 285 K, with a well-defined valley around 285 K. This provided the rationale to call all pixels colder than 285 K cloudy. The scale dependent statistics presented in the bulk of this paper are restricted to these cloudy pixels.

Because of the uncertainties involved in clear sky classifications as well as the satellite instrument noise we decided not to include one- and two-pixel clouds in our analysis. This choice will later be justified further when we indicate (in Figures 5 and 6) that the minimum T of a large portion of these small clouds are indeed, very close to the clear sky threshold of 285 K. The one- to two-pixel isolated clouds are close to the resolution of the instrument and hence are subject to a large uncertainty. Recall that the area of each pixel is 35 km^2 and that the nadir instrument resolution in the IR channel is 25 km^2 and significantly higher toward the satellite's limb. Instead of describing the effects of one- and two-pixel clouds under the various cloud categories, we discuss their combined effects under the category "small clouds." The adopted scene classification can be summarized as follows:

Overcast

$$T \leq 285 \text{ K} \qquad N \geq 3 \text{ pixels}$$

Overcast—small clouds

$$T \leq 285 \text{ K} \qquad N \leq 2 \text{ pixels}$$

Clear and/or partially cloudy

$$T > 285 \text{ K}$$

where N denotes the number of pixels. The above scheme is referred as the base case (BASE). For the bulk of the results presented here we do not attempt to distill the purely clear scenes from the last category above. The fundamental difficulty we face is to distinguish the partially filled (or broken) boundary layer clouds from the marine aerosols, both of which enhance the visible albedo and have minimal effects on T [*Wielicki and Parker*, 1992; *Lin and Coakley*, 1993]. Because of our interest in analyzing diurnal variations in cloud statistics the visible channel could not be used for the bulk of our analyses since that would skew the results between daytime and nighttime.

To determine the ramifications of choosing the BASE case on our results, we performed a sensitivity study using two other clear sky classification schemes (section 4.3). In one (referred to as $T > 290$ K) we identify clear pixels as those with $T > 290$ K, which is similar to the value adopted by *Liu et al.* [1995] for the tropical Pacific. In the second scheme (referred as bispectral) we retain the $T > 285$ criteria but add the constraint that the visible albedo a_{nb} of clear sky pixels shall not exceed the solar zenith angle dependent directional albedo for clear skies (Figure A1). These directional albedos were computed from the GMS BDM (Appendix A).

In summary, our approach is quite conservative: we use only the overcast clouds of scales larger than 100 km^2 for the scale dependent statistics. For scales less than 100 km^2 we need instrument resolution similar to that of the advanced very high resolution radiometer (AVHRR) on the geostationary platforms. As shown later, the small clouds covered less than 3% of the total area for the BASE case.

3.2. Detect and Spread Cloud Identification

Here we introduce a cloud identification scheme based on the assumption that individual clouds are distinct systems as long as their cores or optically thicker centers are separated by optically thinner or, in our case, higher effective brightness temperature regions. This method provides much more that just cloud amount for different cloud types. For example, it can be used to establish for different cloud types the number of clouds within different size bins. This iterative recursive two-stage cloud identification scheme is called detect and spread (DAS). A general description of DAS is given in section B1, while the specific instantiation used in this study is presented next. DAS is applied to the T field to identify pixels belonging to the same cloud. Two guidelines must be considered before we do so: (1) Detection of clouds based on a certain T threshold involves finding consecutive sets of pixels whose T does not exceed this threshold and which have not been assigned to other already identified clouds. Every newly detected cloud receives a unique label. (2) Spreading of clouds to a certain T threshold involves adding edge pixels colder than this threshold to all already identified clouds until no more edge pixels can be assigned to clouds.

The first set of clouds were identified on the basis of a T threshold T_{min} of 240 K. These, say, N1 clouds were each labeled with a different number and in three steps spread to a temperature of 260 K. This means that clouds 1 through N1 were first spread to 246.6 K, then to 253.2 K, and finally, to 260 K. The next set of clouds, say N2, were then detected on the basis of a minimum detection T of 255 K. These resulting N1 and N2 clouds were then all spread to 275 K in, again, three steps. Two more detection steps at 270 K and 285 K were applied together with the corresponding spread stages to 280 K and 285 K, respectively. More specific information regarding DAS as well as some comments on the sensitivity to the particular choices of detection and spread thresholds are provided in section B.1.

In short, detection in this study occurred at 240, 255, 275, and 285 K, while the corresponding spread thresholds were set at 260, 280, 285, and 285 K. Note that DAS reduces to the single detection threshold approaches listed by *Mapes and Houze* [1993] if only the first detection stage is performed. In these cases a one-pass implementation that is more efficient than the recursive one proposed herein can be used [*Mapes and Houze*, 1993].

Spreading stops when all edge pixels of the current cloud are clear, are too warm, or have already been labeled with a different cloud label number. The set of clouds obtained after two detect and spread cycles is illustrated in Plate 2, where each individual cloud is assigned a random color. We clearly see the effect of spreading between Plate 1b (after cycle 1) and Plate 1c (after cycle 2): many clouds have been spread to occupy larger areas. Note that the final size of a particular cloud may not be reached until the last spread cycle is completed.

Justification for using 240 K as the first detection threshold is based on the assumption that all connected pixels with a T of 240 K or less are associated with one convective system [*Mapes and Houze*, 1993]. On the warm end the final detection and spread thresholds were set to the 285 K clear sky threshold established in section 3.1. The consequence of this cutoff is that very warm clouds, optically very thin cirrus, or small broken clouds may have been ignored and that some cloud edge pixels were not included. Again, ramifications of the adopted clear sky scheme are discussed in section 4.3.

Optically thin cirrus at high altitudes can easily be mistaken for lower level clouds, especially if only one IR channel is available, since optically thin cirrus at high altitudes is often registered at T much higher than expected based on its altitude alone. If these thin cirri are connected to a colder core, DAS will associate them with this core. While situations can be sketched where such an association will not be performed correctly, DAS remains a valuable approach to solving such complicated cases. Detached cirrus poses a difficult problem for our one-channel implementation, especially if its T is close to that of the clear sky. In the case of AVHRR data [*Kidwell*, 1991], thin cirrus can be distinguished from low level clouds by their difference in the channel 4 and channel 5 effective brightness temperatures as a function of the channel 4 effective brightness temperature [*Lin and Coakley*, 1993]. As advocated in section B1, such additional distinctive features should be included in the DAS scheme to guide selection of detect and spread subfeature domains that represent different cloud classifications, thus strengthening DAS's cloud differentiating ability. These more rigorous approaches to cloud detection are not pursued in this paper.

3.3. Cloud Classification

Identified clouds were classified into seven cloud types on the basis of the effective brightness temperature criteria listed in Table 1. At least three pixels (about 35 km^2 each) had to satisfy these temperature criteria in order for a cloud to be classified as such. By imposing this three-pixel requirement a considerable area of a cloud had to be cold enough to satisfy the temperature criterion, thus making the analyses less sensitive to spuriously low effective brightness temperatures. Recall that clouds smaller than three pixels were not used in obtaining the scale dependent statistics described below.

All clouds whose core has at least three pixels colder than 219 K are defined as deep convective (DC) clouds. Two types of deep convective clouds are defined: mesoscale convective systems and non-MCS systems. The MCS scheme is adopted from *Laing and Fritsch* [1993]: it must have a core with a brightness temperature less than 219 K and an area greater than 50,000 km^2; the core must be surrounded by anvils with brightness temperatures less than 240 K; the area of the core plus the anvils must exceed 100,000 km^2. Besides the size criteria for MCS, Laing and Fritsch imposed the additional constraint that the aspect ratio of its minor and major axes should exceed 0.7 and that it should last for at least 6 hours. We did not impose these particular constraints in our analyses. Even though an MCS must contain a total area of 50,000 km^2 colder than 219 K, it does not mean that these cold pixels all belong to one cluster within the MCS; they may be distributed over many small cold cores as long as they are connected via pixels colder than 240 K [*Chen and Houze*, 1996].

3.4. Cloud Area Binning

Area binning took place with four bins per size decade between 100 km^2 and 1,000,000 km^2. These areas are related to climate model resolution in Table 2. In order to be able to validate whether these models accurately reproduce the cloud's radiative properties we calculated the narrow band albedos a_{nb} for every pixel and used them to calculate the average albedo per cloud type and the contribution of each cloud type to the total reflected shortwave flux from the cloudy portion of the scene, again as a function of cloud area. The average cloud albedo a_{nb} of a particular cloud type c_t is defined as the total outgoing shortwave flux over the total incoming flux of all daylight pixels:

$$a_{\mathrm{nb}}c_t = \frac{\sum_{i=1}^{N_{\mathrm{day}}} a_{\mathrm{nb}}c_{t_i}S_0(\mu_{0_i})}{\sum_{i=1}^{N_{\mathrm{day}}} S_0(\mu_{0_i})}$$

whereby N_{day} is the total number of daylight pixels over all clouds of type t and $S_0(\mu_{0_i})$ is the incident solar top of the atmosphere (TOA) irradiance at cloudy pixel i. To provide scene statistics, the average area and albedo were calculated for each cloud type and are tabulated in Table 3.

3.5. Diurnal Statistics

The diurnal variability of the mean area as well as area-weighted mean T and a_{nb} were calculated for all of the cloud types in Table 1. These statistics were obtained by determining for every cloud its centroid's local hour bin and using it to update that bin's total cloud type statistic. A similar procedure was used to obtain the number of occurrences statistics.

Since the GMS shut itself off during 1330 and 1430 UT and since some images were corrupted in the transmission process, certain local hours were sampled more frequently than others. This shut-off is clearly indicated in Figure 2 (right) in that it shows a gap around 1400 UT. Figure 2 is explained below. To account for this nonuniform sampling in our frequency distribution statistics, we calculated for all 24 local hour bins the total area that was observed within our domain summed over all 30 days. A local hour bin corresponded to a 15° longitudinal swath around the longitudes that correspond to whole hours (e.g., 150°E, 165°E, 180°E). Every image $I(t_g)$ at a particular UT hour t_g holds area slices $A(t_l)$ of maximally 15° wide around local hours t_l in the range $[t_n, t_m]$ where t_n and t_m are functions of t_g with $n, m \in [1, 24]$. In order to obtain accurate measurements of the true number of clouds $N(c(t), t_l)$ of a particular type at a given local hour one needs to know the total area observed at that hour $A(t_l) = \Sigma_i A_i(t_l)$ versus the maximum total area $A_{\max}$ observed across all local hours; $A_{\max} = A(t_k)$ where $k = \mathrm{argmax}_l A(t_l)$. Given the computed number of clouds $M(c(t), t_l)$ of a particular cloud type at a given local hour, the area sampling corrected estimate $N(c(t),$

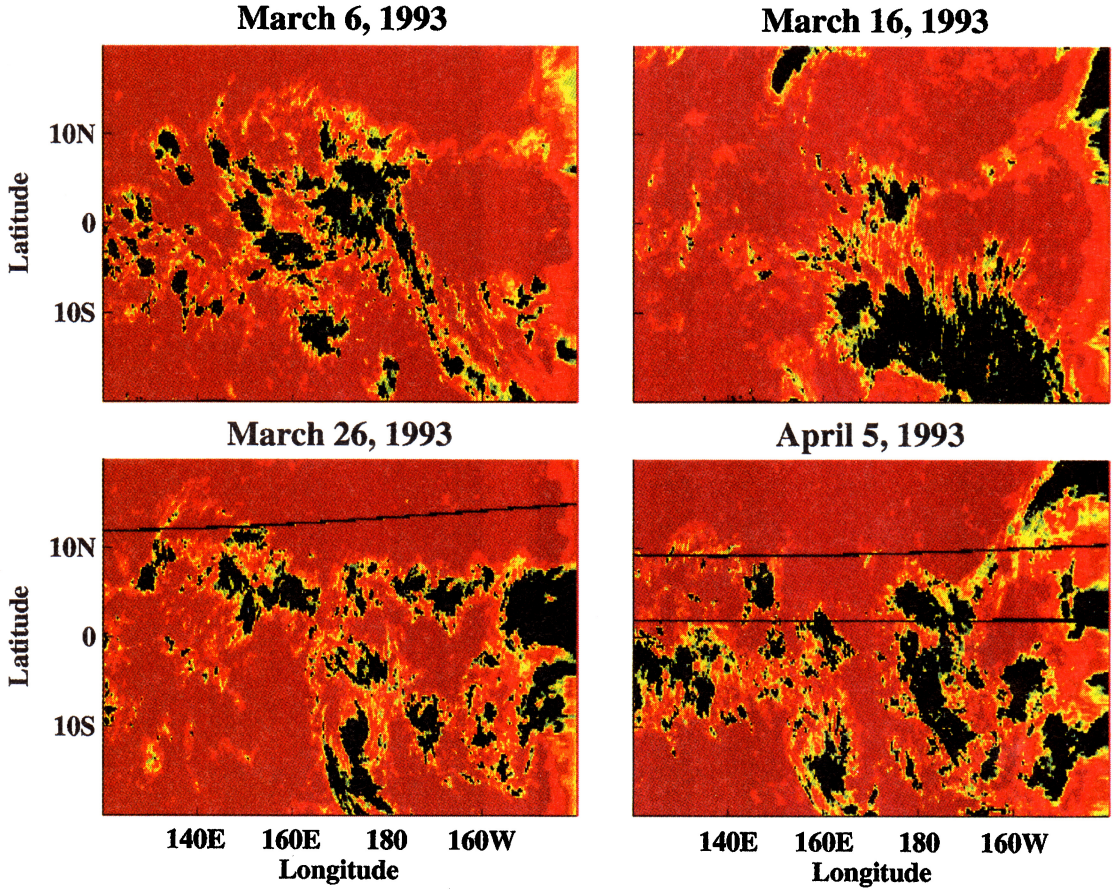

Plate 1. Noontime GMS effective brightness temperature images. Black indicates colder than 240 K, while dark red indicates warmer than 285 K.

t_l) is obtained with $N(c(t), t_l) = \lambda(t_l)M(c(t), t_l)$, where $\lambda(t_l) = A_{max}/A(t_l)$. The values for $\lambda(t_l)$ are shown in Figure 1. It is clear that local hour 2 was sampled less frequently than hour 7, for instance, which was to be expected since it corresponds to 1400 UT around which time no observations were made.

To assess whether the GMS exhibited any systematic bias in its clear sky brightness temperature observations, the average clear sky brightness temperatures were computed as a function of local hour as well as UT observing time. Since the objective here is to identify pixels that are free of any cloud contamination, a more stringent clear sky criterion was adopted than the one presented in section 3.1. The essential elements of this modified scheme are $T > 290$ K; the standard deviation of T for the pixel of interest and the eight surrounding pixels is less than 0.6 K (the noise level of the instrument [*Senta*, 1989]); and all of its eight surrounding pixels also satisfy these two criteria. The resulting averages are shown in Figure 2. It is clear that GMS registers significantly higher (by almost 2°) clear sky brightness temperatures shortly after the Sun no longer shines into the satellite's field of view (after the satellite resumes observation). Besides the apparent instrument-induced temperature spike around 2400 LT, a clear diurnal cycle is observed in which T increases by about 0.5 K around noon and decreases again around midnight. To what extent the 2° temperature spike is the result of satellite heating/cooling remains to be determined, but it is clear that such large changes in temperatures will have some effect on the cloud distributions obtained by using DAS. The expected consequences of this effect were examined through the sensitivity study described in

Table 1. Cloud Type Area and Temperature Specifications

Cloud Type	Area Characteristics
MCS	($T < 219$ K) > 50,000 km^2; ($T < 240$ K) > 100,000 km^2
Deep convective	($T < 219$ K) > 103.8 km^2 (i.e., three pixels)
Mixed 1	219 K < T_{min} < 230 K
Mixed 2	230 K < T_{min} < 240 K
Mixed 3	240 K < T_{min} < 250 K
Mixed 4	250 K < T_{min} < 270 K
Low clouds	T_{min} > 270 K

T_{min} is the effective brightness temperature of the third coldest pixel.

Table 2. Equatorial Grid Cell Dimensions Corresponding to Several Commonly Used Climate Model Resolutions

Model	Number of Grid Cells, Longitude by Latitude	Grid Box Size, deg	Equatorial Grid Box Size, km^2
T21	64 × 32	5.625	313,600
T42	128 × 64	2.8125	87,400
T63	192 × 96	1.875	34,845
T106	320 × 160	1.125	12,544
T213	640 × 320	0.56	3,136

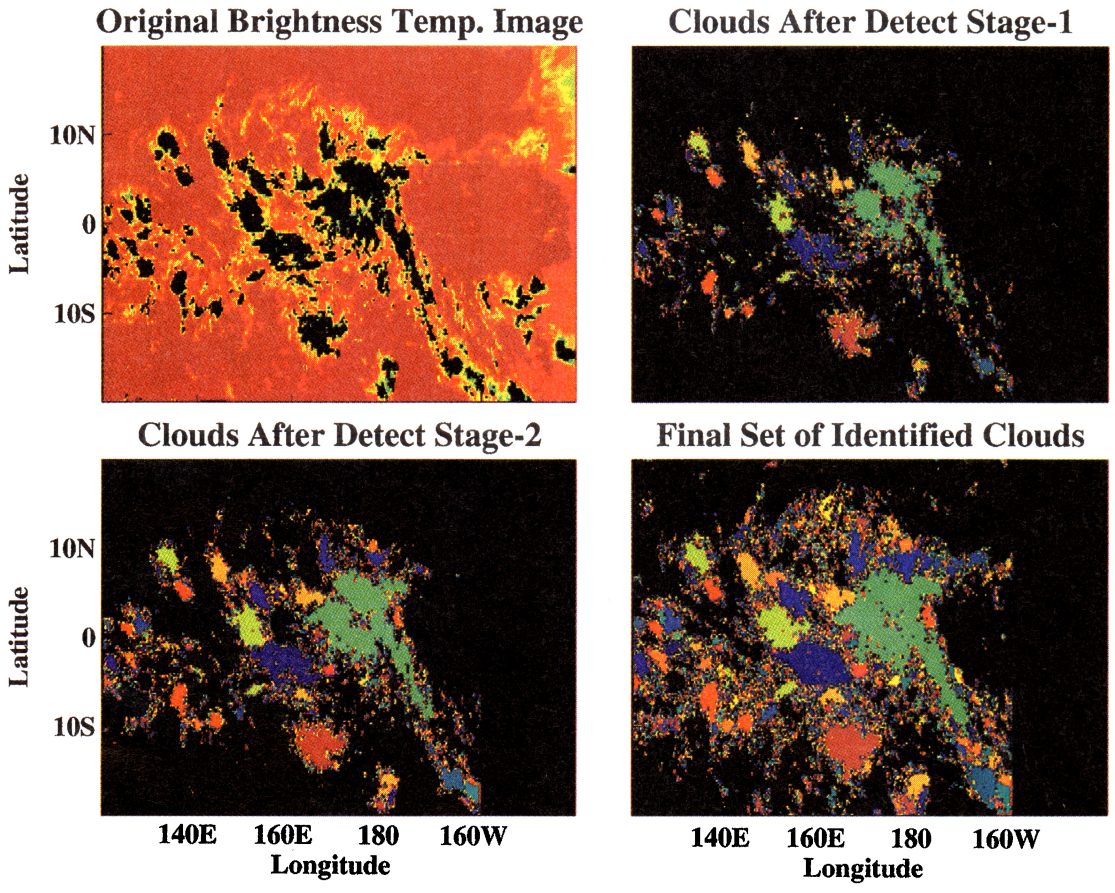

Plate 2. March 6, 1993, effective brightness temperature image with the identified clouds after the first and second detection stage plus the final set of identified clouds. In Plate 2a, black indicates colder than 240 K, while dark red indicates warmer than 285 K. In Plates 2b, 2c, and 2d, each individual cloud is assigned a random color.

section 4.3, which revealed that different clear sky classification schemes have only a marginal impact on our results.

3.6. Tracking Mesoscale Convective Systems

An automatic cloud tracking algorithm (CTA) was developed to follow the time evolution of size as well as average radiative ($\bar{T}$ and $\bar{a}_{ab}$) characteristics of MCS. Besides calculating characteristics such as spatiotemporal frequency, area, and lifetime we also looked at the local hour at which they attained and lost their MCS status and when they reached their maximum area.

In the CTA, MCS are first replaced by their ellipsoidal equivalents. These ellipsoids have the same centroid, aspect ratio, area, and orientation as the underlying MCS. Tracking is then performed on these ellipsoids by allowing for merging and splitting. One particular MCS's time series consists of a collection of MCS that through splitting and merging form one single system at least once. This algorithm differs slightly from the one used by *Williams and Houze* [1987] in that tracking is performed on ellipsoids thereby significantly reducing the system's computational and memory load since it no longer requires cloud masks in computing cloud overlap. See section B.2 for details on CTA.

The present version of CTA may not be applicable to time series with sampling periods greater than several hours because MCS may travel too far to assure accurate association. This is also the reason why small clouds cannot be tracked with this overlap-based scheme. More sophisticated schemes such as those used in tracking ice floes need to be used in order to track small clouds across longer time intervals [*Kwok et al.*, 1990]. Such an extension was not pursued.

4. Results and Discussions

4.1. Statistics Required for Parameterization

The cumulative contributions of various cloud sizes to the percent cloud area coverage and to the cloudy sky albedo are shown in Figures 3 and 4. Uncertainties in the size due to cloud edge effects and due to partially filled pixels are expected to be large for small clouds, which are conservatively taken to be those with sizes less than 1000 km^2. Hence we have shaded the region less than 1000 km^2 as "gray" in all of the figures. The climate model resolutions are indicated on top of each of the figures by T42, $\cdots$, T213. These indicate the resolution of spectral GCMs in terms of series of surface spherical harmonics with a so-called triangular (hence the letter T) truncation scheme for the longitudinal and latitudinal wave numbers. Since resolution of GCMs can vary with latitude (as in the case of spectral GCMs), the values shown are based on their equatorial grid cell size (also see Table 2).

A summary of Figures 3 and 4, in terms of the total domain (20°N to 20°S and 120°E to 160°W), is given in Table 3. The values are diurnally (all 22 observing hours for cloud cover and

Table 3. Area and Narrow Band Albedo Statistics for Every Cloud Type

	Deep Convective		Mixed Cloud Types				
	MCS	Non-MCS	Mixed 1	Mixed 2	Mixed 3	Mixed 4	Low
Fraction of cloudy area, %	26	25	11	13	9	9	7
Average narrow band albedo, %	34	28	22	21	20	21	23

The average cloud cover is 42%. The fractional cloudy area for each category is normalized with 42%. See Table 1 for the T ranges used for the mixed cloud types.

daylight hours for albedos) averaged quantities, averaged over the 31 days between March 7, 1993, and April 7, 1993.

The total cloud coverage (not including the one- and two-pixel clouds) for the domain is 42% with a mean visible albedo of 26.6%. The small clouds (one and two pixels) occupied 3% of the total area with a mean visible albedo of 31% and a mean T of 241 K (BASE case in Table 4). The cold T and high visible albedo suggest that these small clouds are primarily convective clouds. The distribution across all seven cloud types is presented in Table 3. Roughly half the cloudy area was covered with deep convective systems, and the DC systems' average albedo of about 32% was more than 10% higher than that of the non-deep convective (other) cloud types at about 21%. Of these deep convective systems, slightly more than half were covered with MCS, which have an average albedo of 34% versus 28% for the non-MCS deep convective clouds. The average albedo of all other cloud systems (including the low clouds) was about 21% and did not differ substantially from one type to the other.

The cumulative distributions shown in Figures 3 and 4 indicate the following: (1) More than 95% of the deep convective cloud contribution to the total area covered by deep convective clouds (MCS and non-MCS) are from clouds with area greater than 10^4 km^2. Likewise, deep convective clouds with area greater than 10^4 km^2 contribute 95% of the albedo of all deep convective clouds combined. (2) The reverse is true for the low warm clouds. About 80% of the contribution to fractional cover and albedo is due to small-scale clouds (area less than 10^4 km^2). (3) The other mixed cloud types fall in between the convective and low clouds. (4) The cumulative contribution to the total cloud reflected visible radiation flux (Figure 4) indicates that the two deep convective cloud types (MCS and non-MCS) were responsible for about 63% of the total daily cloud reflected solar energy. Note that this does not include the portion reflected by clear sky pixels. By including the two coldest mixed cloud types the total contribution of these convection-related clouds was about 81.5%.

The percentages cited above will change slightly if the one- to two-pixel clouds are included in the statistics. The number of clouds in each size bin, the albedo, and the effective brightness temperature distributions per cloud types as a function of cloud area are shown in Figures 5 and 6. These distributions were used to calculate the cumulative contributions shown in Figures 3 and 4. The statistics were only calculated if more than 20 clouds (in a month) of a given type and size were observed.

Figure 5 shows characteristic sizes for each cloud type as indicated by the peaks in the parabolic curves. Non-MCS deep convective clouds show a distinct peak at about 20,000 km^2. The characteristic size decreases with an increase in the cloud top temperature. These distributions are critical for parameterizing clouds that are too small to be resolved by the model.

Figure 6a indicates that the average MCS effective brightness temperature did not change considerably with area. The same holds for large (i.e., area >10,000 km^2) non-MCS deep convective clouds. On the other hand, larger non–deep convective clouds are associated with warmer average effective brightness temperatures, which is indicated by the fact that all lines point to the upper right. Similar dependencies are observed between the average albedo and area: albedo decreases for most non–deep convective systems except for mixed 4 (warmest) and low clouds (Figure 6b). Note the enhanced albedo of small non-MCS and mixed 1 (219–230 K) cloud types. One possible explanation for the dependencies revealed by the mixed 1–3 clouds is that their optical depth may be decreasing with the size; as a result, the effective brightness temperature increases (penetration of clear sky emission) with size, and albedo decreases with size. A second more consequential explanation is that these large mixed clouds are truly

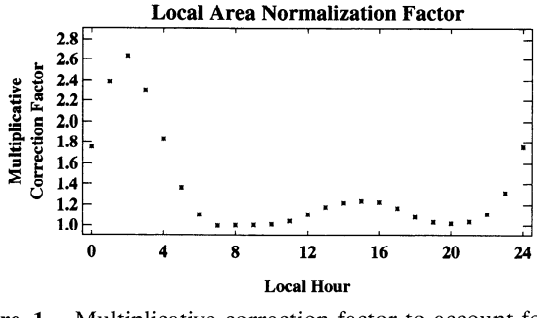

Figure 1. Multiplicative correction factor to account for the fact that each local hour is not sampled equally often. This factor was used to obtain the cloud frequency distributions as a function of local hour in Figure 10.

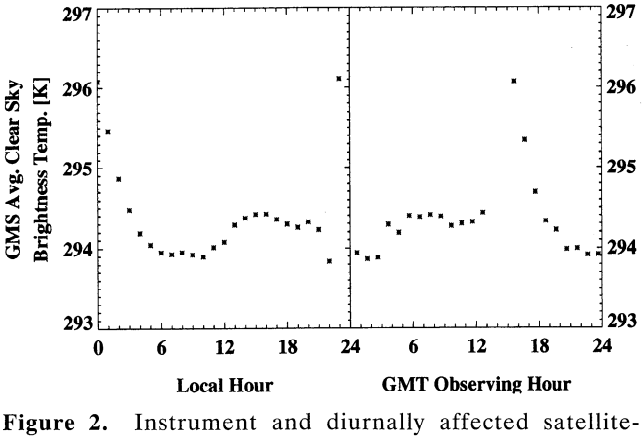

Figure 2. Instrument and diurnally affected satellite-retrieved clear sky temperatures. Average clear sky temperature as a function of UT observing hour as well as local hour.

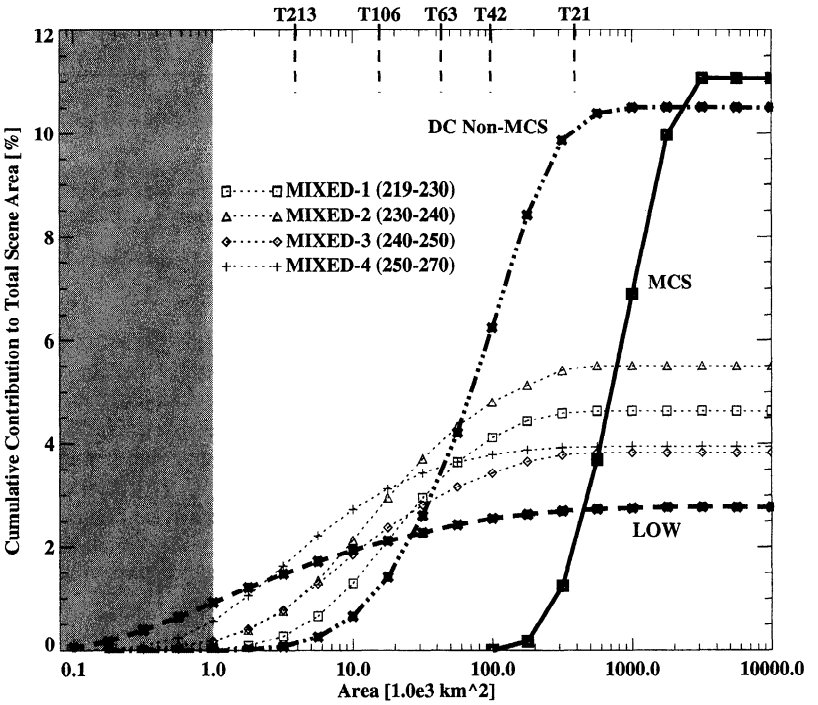

Figure 3. Cumulative contribution of each cloud type to the total percent cloud area coverage as a function of the cloud area. The monthly total cloud cover was 42%. The data for all clouds are between 20°N and 20°S and 120°E and 160°W.

a collection of mixed clouds separated by pixels partially filled with mixed clouds. While this seems unlikely based on the fact that DAS breaks cloud decks up into smaller segments if sufficiently large fluctuations in T exist, to obtain a definitive explanation, a detailed sensitivity using many different DAS thresholds is needed, and other data sources need to be folded into DAS as suggested in section B1.

Low clouds differentiate themselves from other non–deep convective clouds: larger ones are more reflective instead of leveling out at an albedo of about 22%. This is largely an artifact of the applied clear/cloudy criterion, as will be shown below. Furthermore, if we simply extrapolate the trends in Figures 5 and 6 (discussed below) down to smaller-scale clouds, we see that a large portion of these small clouds are predicted to occur around 285 K, suggesting uncertainty about their true nature.

4.2. Temporal Statistics Required for Validation

Our main focus will be directed toward MCS and non-MCS cloud types because of their large area and cloud albedo contributions. Diurnal variation in cloud properties and lifetimes of clouds cannot be tuned; they have to come out of the model simulation. Hence the temporal statistics can be used for rigorous validation.

Figure 7a shows normalized frequency (number of clouds at a local hour normalized by the maximum number of cloud occurrences for that cloud type over all 24-hour bins) of occurrence. MCS ensemble number frequency peaks in the early morning (around 0500 LT), which is generally associated with organized weather disturbances that facilitate more intense deep convection [*Gray and Jacobson*, 1977]. Non-MCS have a double peak, one at about 0400 LT and the other at about 1600 LT. The first peak is most likely the result of an increased number of new convective cells similar to those in MCS, while the latter peak is attributed to large MCS splitting up into the smaller non-MCS. Number distributions alone are not sufficient. Diurnal variation of total cloud area normalized by the maximum total cloud area observed over all 24-hour bins is shown in Figure 7b. The normalized total area follows the diurnal pattern of the number frequency shown in Figure 7a. This is consistent with those reported by *Mapes and Houze* [1993]: deep convective areas show a distinct area increase just before sunrise.

It is interesting to note that while MCS decrease in total area and frequency between sunrise and midnight, the frequency and total area of smaller convective systems with a 219 K core peaks again around midafternoon. This nicely shows that many MCS that lose their MCS status (decrease in consecutive area within 240 K contour) turn to non-MCS DC. This distinct second peak in non-MCS is not observed in other studies, which may be due to the fact that we look at a cloud's total area and not just at that portion colder than some convection-related cold temperature. To capture fully the mechanisms involved, one needs to look at the number of convective cells ($T < 219$ K) in an MCS as well as their area as a function of time [*Chen and Houze*, 1996]. While not pursued any further, we note that studying such interactions is greatly facilitated by a cloud detection scheme such as DAS.

Individual MCS were tracked over time with the CTA algorithm described in section 3.6. The area characteristics for all MCS that survived more than 3 hours are shown in Figure 8. Both panels indicate roughly that the maximum and average areas increase with cloud lifetime. Larger cloud systems have longer lifetimes. This is consistent with findings during the Tropical Ocean-Global Atmosphere Coupled Ocean-Atmosphere Response Experiment (TOGA COARE) [*Chen and Houze*, 1996]. Several instances of MCS that lived longer than

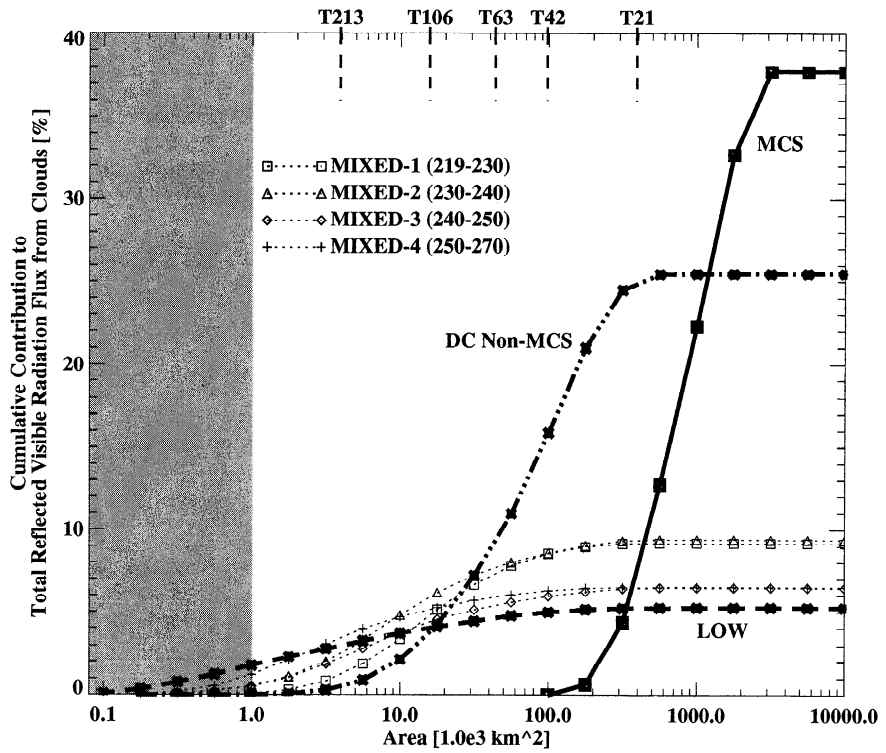

Figure 4. Cumulative contribution of each cloud type to the total reflected visible radiation flux as a function of the cloud area; the average cloud albedo was 26.6%.

100 hours were found, two of which are shown in Figure 9. The day D and night N size fluctuations, particularly those in Figure 9b, are consistent with the ensemble diurnal variations shown in Figure 10.

For all MCS, their local start and end times were calculated as well as the time at which they reached their maximum area (Figure 10). It is clear that most MCS are born between 0200 and 0500 LT while they reach their maximum area around 0400 and around 1700 LT. They seem to lose their MCS status slightly more often between 0800 and 2000 LT, which is consistent with the earlier remark about non-MCS DC also occurring more frequently in this time frame (shrinking MCSs turning into non-MCS DC).

4.3. Sensitivity Studies

Statistics such as those shown in Figures 3–10 can be quite sensitive to the algorithm employed for deriving the clear skies. Furthermore, the detect and spread algorithm is also sensitive to the threshold temperatures used to separate various clouds. We have performed numerous sensitivity studies. The results from applying the three different clear sky detection schemes described in section 3.1 (Table 4) are presented next (Figure 11). The comparison was performed on all noontime scenes because the bispectral case could be applied during daylight hours only. As a reminder, the BASE case was used as the basic scheme in this paper.

Table 4. Sensitivity of the Cloud Cover and Albedo to Clear Sky Algorithms

Variable	BASE Case	$T > 290$ K	Bispectral
Overcast criteria T	<285 K	<290 K	<285 K; $a_{nb} > a_{nb}$ (clear)
Overcast*			
Cloud cover, %	40	53	60
Albedo, %	25	21	22
Effective brightness temperature, K	258	266	269
Overcast—small clouds†			
Cloud cover, %	3	8	5
Albedo, %	31	20	24
Effective brightness temperature, K	241	264	264
Clear and/or partially cloudy			
Cloud cover, %	57	39	35
Albedo, %	9	8.6	5.5
Effective brightness temperature, K	291	293	292.5

The values shown are for local noon only.
*$N \geq 3$ pixels.
†$N \leq 2$ pixels.

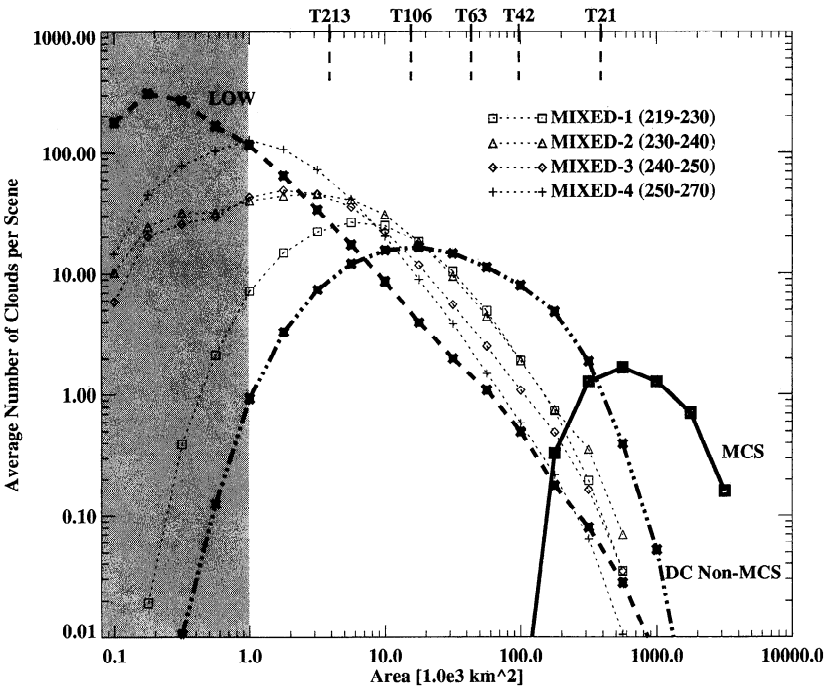

Figure 5. Number distribution of clouds as a function of their area.

The main change in cloud statistics from BASE (i.e., 285 K) to 290 K to bispectral was an increase in total cloud area. In addition, the size distributions for all cloud types shifted to slightly larger sizes (Figure 11), indicating that every cloud increased in size. This was to be expected because the edges of most clouds (not those already surrounded by other clouds) were extended into regions previously called clear. As a result, the total cloud fraction increased, and the average cloud albedo decreased, as indicated in the last two columns of Table 4. While not shown here, the bispectral case also showed a significant decrease in the number of small (<1000 km^2) low clouds with a higher resulting albedo of 22%. The 15% albedos of the large low clouds it produced were neither too large (as with BASE) nor too close to the clear sky value (as with 290 K). We believe that the three cases considered in Table 4 bracket the range of uncertainty due to clear sky algorithms.

In spite of the fact that the total cloud cover increased from 43% to 65% between the BASE and bispectral cases, the cumulative contributions to the total cloudy area and the reflected visible radiation flux across the seven cloud types were nearly identical between the three cases described in Table 4 (compare Figures 11a, 11b, and 11c). In summary, as is well known, the total cloud cover and corresponding cloudy albedo are quite sensitive to the adopted clear sky scheme. However, the overall conclusions derived from the statistics shown in Figures 3–7 are quite insensitive to the clear sky scheme.

5. Conclusion

A satellite-based cloud identification scheme to detect individual clouds was used to obtain scale dependent cloud properties as well as diurnal variations of different cloud types. This scheme enables us to label clouds as separate even if they are separated by an optically thin region or broken pixels. We also introduced an algorithm to automatically track the time evolution of the mesoscale convective system, thus providing insight about the lifetimes of individual systems.

While we realize that our 1-month data set may not be a climatologically representative sample, it is sufficient for demonstrating the usefulness of the present approach for guiding the development and evaluation of GCMs. Evidence for large seasonal variations in the number of MCS is, for example, given by *Nakazawa* [1988] and *Laing and Fritsch* [1993]. Furthermore, our results are applicable only to the tropical Pacific cloudiness. Generalization to other regions must await detailed comparison with results from the other tropical regions. Given these caveats, let us explore how our satellite statistics could be used to guide the development and evaluation of cloud parameterizations in GCMs. In terms of the radiative importance of resolvable and fully parameterized clouds for different GCMs we make the following inferences from Figures 3 and 4.

1. A T213 GCM should resolve explicitly 85% of the radiatively important cloudiness (MCS, non-MCS DC, mixed 1 and mixed 2); a T106 GCM should resolve about 70%; a T42 GCM should resolve about 45%; and a T21 GCM can resolve about 30%.

2. A T213 model should resolve 95% of the radiatively important deep convective (MCS, non-MCS DC) cloudiness; a T106 should resolve about 90%; a T42 should resolve about 70% (100% of MCS); and a T21 will resolve only about 35% of the radiative effect of deep convective cloudiness.

3. T21 and T42 GCMs cannot resolve any of the low clouds, while the T213 can resolve as much as 30% of the total low cloudiness. Recall that since the satellite cannot see low clouds below a thick upper level deck, the low clouds shown in our statistics are primarily those that are not overshadowed by a convective system. One example of the low clouds observed in our study is the trade wind cumulus clouds. Our statistics here reveal that such low clouds (because of their smaller cloud cover) have only a small contribution to the overall albedo for this region.

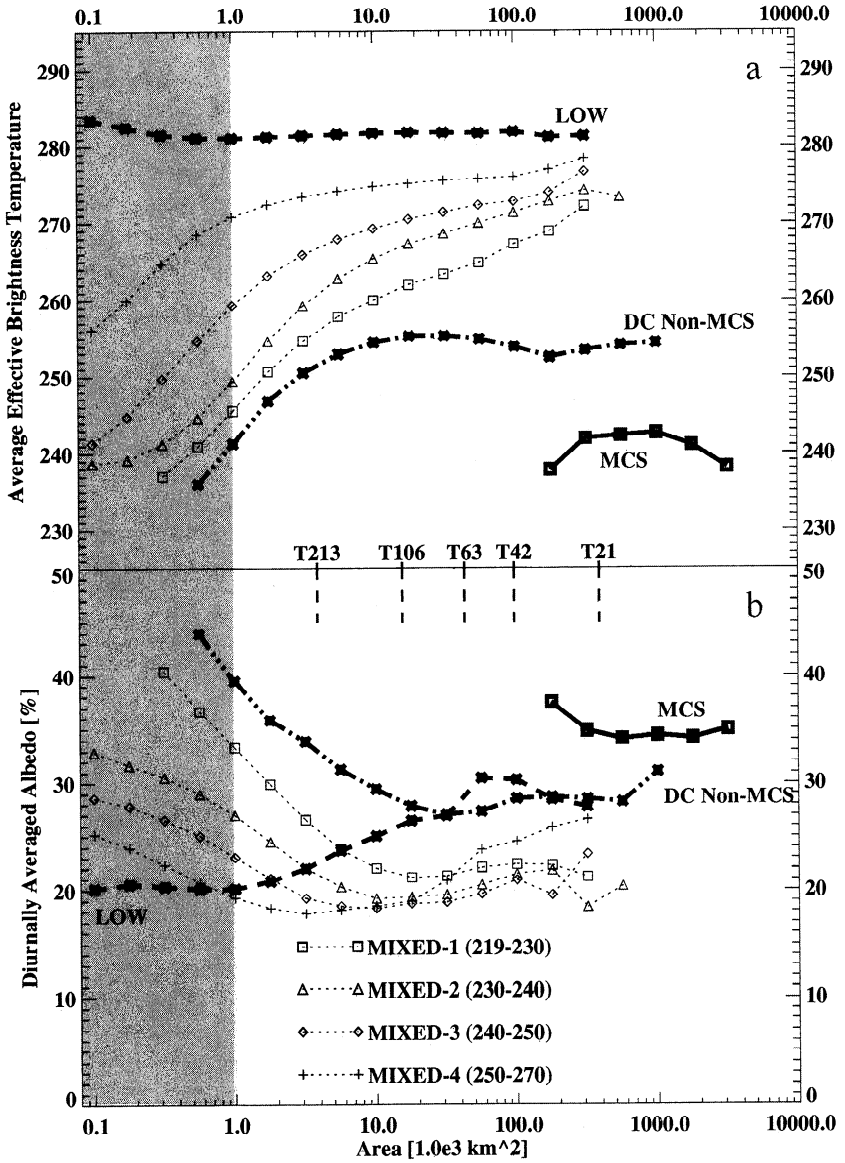

Figure 6. (a) Average effective brightness temperatures for each cloud type as a function of cloud area. (b) Average diurnally averaged cloud visible albedo for each cloud type as a function of cloud area.

As indicated, a T213 model should resolve almost all of the radiatively important clouds. In other words, a T213 should simulate the static and temporal statistics shown in this paper. Referring to Figure 5, we note that it will not be able to resolve most of the small-scale convective clouds since scales less than that of the T213 dominate the population (number density) of clouds. This skewed distribution does not influence the average albedo since it is dominated by the bigger clouds. However, the small-scale clouds may dominate transport of mass and momentum, particularly in the case of the cumulus clouds. Furthermore, even for the large-scale non-MCS and MCS clouds, parameterization requires treatment of small-scale unresolved cumulus elements, which contribute most of the condensate and vapor to the larger-scale mesoscale circulations [*Leary and Houze*, 1979; *Mapes*, 1993; *Chen and Houze*, 1996]. In summary, even a T213 would require some sort of cumulus parameterization for mass and momentum transport, an issue which is beyond the scope of this paper.

Strong diurnal variations in the number and the area of deep convective systems were observed in the whole ensemble. These diurnal variations were also shown to exist in the time evolution of individual MCS. Even though we used a significantly different cloud detection scheme, these variations were shown to match closely those found by others. Since diurnal variations in cloud properties cannot be tuned, they have to come out of the model simulations. Hence temporal statistics can be used for rigorous validation.

We have shown how the cumulative area and radiative contributions in Figures 3 and 4 can be used to assess the relative importance of clouds at resolvable and subgrid scales while the radiative properties of these clouds at different scales, which are important in guiding cloud parameterization, can be read from data such as that shown in Figure 6. Finally, the diurnal and time evolution statistics in Figures 7–10 as well as the scale dependent statistics in Figures 3–6 are instrumental in validating the model simulations. Again, recall that our findings are limited to the tropical Pacific case and that the radiative mea-

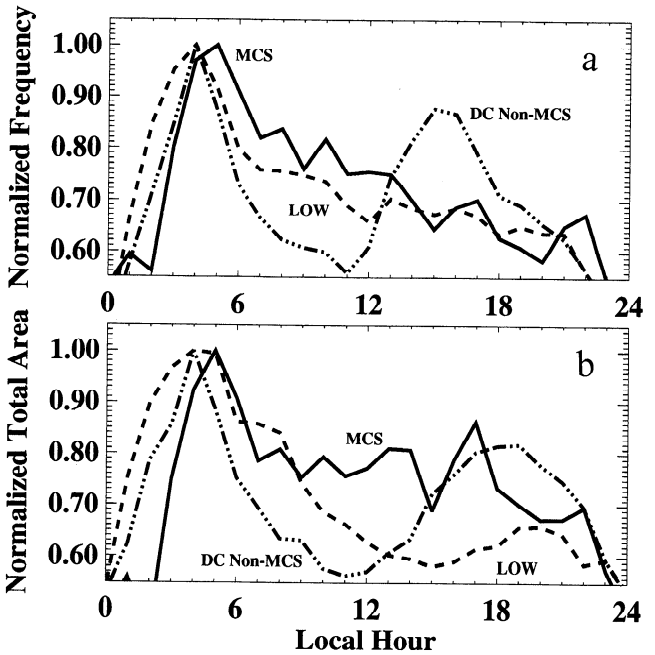

Figure 7. (a) Number of clouds of a given cloud type normalized to the maximum number of these clouds observed across the 24-hour bins. The average number of clouds of each type per scene are 5 MCS, 97 non-MCS, 135 mixed 1, 336 mixed 2, 299 mixed 3, 627 mixed 4, and 1174 low. (b) Total area of a given cloud type normalized to the maximum total area that these clouds occupied across the 24-hour bins.

surements from GMS should ideally be calibrated against known reference sources.

The Lagrangian approach presented is an illustration of how the satellite data can be used to explore objective parameterization and validation of clouds in GCMs. We conclude with the cautionary note that we are still at an infancy in our ability to characterize clouds solely from satellite data and that the current scheme may suffer from several limitations because of the lack of calibration or validation with ground truth. A promising new approach has been proposed by *Liu et al.* [1995] that combines microwave data with the IR and visible data. These limitations, however, should not impact the validity of the approach presented here.

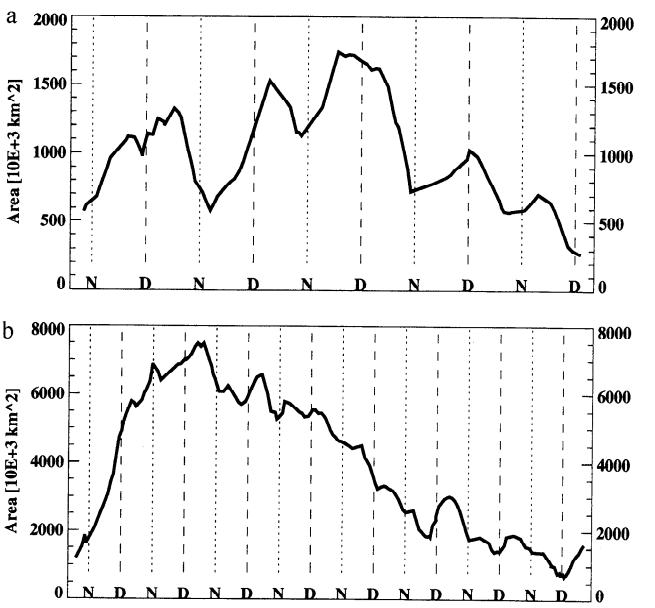

Figure 9. Example of two diurnal area cycles of an MCS that lived almost 5 days. The D and N along the x axis indicate 1200 and 2400, respectively.

Appendix A: Procedure to Convert Observed Radiances to Albedos

Here we present the bidirectional model (BDM) as computed from our 1-month GMS satellite data set and compare it against the Earth Radiation Budget (ERB) BDM. A similar comparison has been made by *Stuhlmann et al.* [1985].

The narrow band visible radiances measured by GMS have to be converted to narrow band visible irradiances (or narrow albedos) before we can characterize the radiative effects of clouds. For this purpose, we need the so-called bidirectional model (or BDM), which relates the radiance $L(\theta_0, \theta, \varphi)$ to the desired irradiance $M(\theta_0)$, where θ_0 is the solar zenith angle, θ is the satellite viewing angle, and φ is the satellite viewing azimuth angle. This relationship also depends on cloud type. The BDM relates L with M according to

$$M(q_0) = \pi L(\theta_0, \theta, \varphi)/R(\theta_0, \theta, \varphi)$$

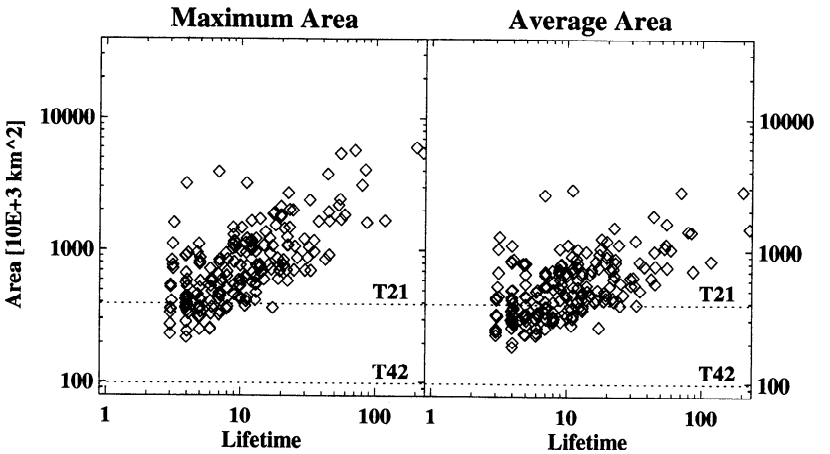

Figure 8. MCS maximum and average areas as a function of cloud lifetimes.

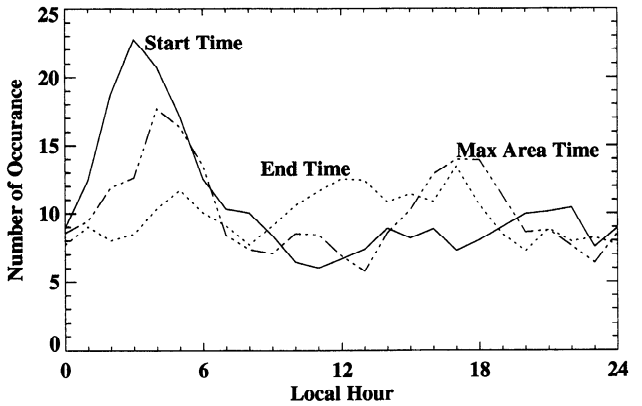

Figure 10. Local hours at which MCS that lived longer than 3 hours started, ended, and reached their maximum area.

where $R(\theta_0, \theta, \varphi)$ is referred to as the anisotropic factor. The next step is to find the bidirectional function $R(\theta_0, \theta, \varphi)$. Note that instead of using $L(\theta_0, \theta, \varphi)$ and $M(\theta_0)$ one can equivalently substitute reflectivity $r(\theta_0, \theta, \varphi)$ and albedo $a_{nb}(\theta_0)$ (narrow band in our case) since $r(\theta_0, \theta, \varphi) = L(\theta_0, \theta, \varphi)/S_0$, where S_0 is the top of the atmosphere solar irradiance.

The procedure for obtaining $R(\theta_0, \theta, \varphi)$ is the same as that described by *Suttles* [1986] for the Earth Radiation Budget Experiment (ERBE). We base our cloud classification on effective brightness temperatures T. For the extended tropical Pacific scene (120°E–140°W; 20°S–20°S) we bin the observed 30 days of hourly radiance $L(\theta_0, \theta, \varphi)$ with respect to T, θ_0, θ, and φ. The incremental steps used for this binning are given in Table A1. Bins with less than 1000 observations, which occurred because of our limited region and time frame, were filled using linear extrapolation/interpolation of surrounding filled bins. For each of the T and θ_0 bins we integrate $L(\theta_0, \theta, \varphi)$ with respect to the azimuth and satellite zenith angle to obtain $M(\theta_0)$. The ratio of the computed M with the $L(\theta_0, \theta, \varphi)$ yields $R(\theta_0, \theta, \varphi)$ for each T bin. To obtain narrow band albedos, the instantaneous observed reflectivities need to be divided by $R(\theta_0, \theta, \varphi)$. The fundamental assumption in using T as an index to clouds at different altitudes is equivalent to assuming that all clouds are blackbodies. Since we only had one IR channel available, this is a reasonable assumption.

To assess the validity of the resulting GMS BDM, it was compared with the ERBE BDM. The ERBE BDM was calculated for data from the ERB instrument on board NOAA's Nimbus 7 polar orbitor [*Suttles*, 1986]. The difference in conversion factors between the filtered narrow band GMS 4 visible channel radiance and the unfiltered broad band radiance will cause a small-magnitude discrepancy between the ERB BDM and the GMS BDM up to a solar zenith angle of about 70° [*Xianjin*, 1992]. The directional albedos for both models are shown in Figure A1, and a snapshot of the anisotropic factors for two cloud types at two different solar zenith angles is shown in Figure A2. Considering the spectral differences between the BDMs, their correspondence is extremely good. The only difference is that the GMS BDM shows slightly more features, which may be due to the fact that the ERBE BDM was filtered on the basis of the reciprocity principle [*Suttles*, 1986] plus the fact that we only used data from a small region over a relatively short time frame, thus increasing variability and specificity to a particular region within the satellite's footprint or to a seasonally specific cloud distribution. Overall, similarity between the two BDMs is very good. This is consistent with the finding that Nimbus 7 ERB results can be produced using GOES [*Stuhlmann et al.*, 1985].

One of the intrinsic problems with BDMs for geostationary satellites is that they mask any consistent diurnal variabilities in cloud albedo. For example, if an MCS at a certain cloud top temperature undergoes diurnal changes in albedo, as long as

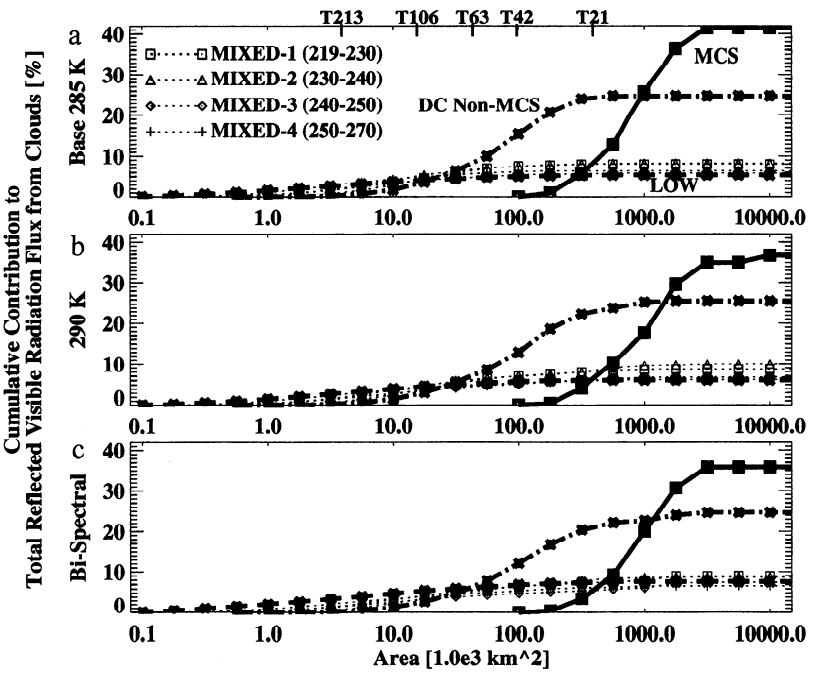

Figure 11. Sensitivity of the statistics to clear sky algorithms. Statistics (described in Figure 4) are shown for the three cases: (a) base; (b) 290 K; and (c) bispectral (see Table 4). The statistics are computed here only for noon (local) time images.

its T stays within a specific T bin, these albedo changes are folded into the BDM as solar zenith angle dependencies and cannot be distinguished from changes in albedo that are solely due to variations in solar zenith angle. One could calculate BDMs by binning the data not by temperature but by altitude, if such information is available, but then the question arises whether the same anisotropic factors can be applied to optically thick and thin cloud segments. BDMs also depend on the angle bin sizes [*Dlhopolsky and Cess*, 1993]. Finally, deriving BDMs from geostationary data is complicated even further by the underlying assumption that the different cloud types occur at all locations in the satellite footprint equally often. An in-depth validation of the GMS BDM would require comparison with data from calibrated instruments as well as inclusion of observations from a larger domain and time span. Such an endeavor is beyond the scope of this paper and is reserved for a separate study.

Table A1. Temperature and Angle Bin Ranges Used to Calculate the GMS Bidirectional Model

Bin	Temperature Range, K	Cosine Solar Zenith Angle, deg	Satellite Zenith Angle, deg	Relative Azimuth Angle, deg
1	180–190	1.0–0.9	0–15	0–9
2	190–200	0.9–0.8	15–27	9–30
3	200–210	0.8–0.7	27–39	30–60
4	210–220	0.7–0.6	39–51	60–90
5	220–230	0.6–0.5	51–63	90–120
6	230–240	0.5–0.4	63–75	120–150
7	240–250	0.4–0.3	75–90	150–171
8	250–260	0.3–0.2		171–180
9	260–270	0.2–0.1		
10	270–280	0.1–0.0		
11	280–290			
12	290–300			

Appendix B: Cloud Detection and Tracking

B.1. Detect and Spread Algorithm

A general cloud detection scheme is introduced followed by the particular instantiation used in our study. Consider an image in which every pixel is attributed with a set of features (e.g., effective brightness temperature, optical depth, albedo). By defining a feature space such that the area around the origin corresponds to clear sky and locations far away to overcast pixels, every pixel can be associated with one point in this space. One can then think of clouds as being represented by regions in this feature space. Cloud classification algorithms are based on this very principle [*Gallaudet and Simpson*, 1991; *Gallegos and Hawkins*, 1993]. In these approaches, points with similar features are clustered and assigned a label (e.g., cloud type). One can then use this to label all pixels in the image by determining to which feature cluster they belong. This, however, does not necessarily provide individual clouds. We therefore decided to explore a slightly different avenue. We start with a cloudy pixel in the image (clear sky pixels are assumed to be masked out first) and then recursively connect it to those adjacent pixels whose features are close. Once no more pixels are near in feature space, a different unassigned pixel is selected, and the process is continued until all cloudy pixels are assigned to some cloud. This raises several questions: what criterion (membership to a particular sub feature domain) should be used in selecting seed pixels; should the same criterion be used to detect all clouds, or should it change as different cloud types (e.g., different cloud top temperatures) are targeted; should spreading of these seeds be completed at once, or should it be performed in stages; if spreading is staged, what criterion should be used to stop spreading? In this study, we explore one possible answer to these questions in the form of the following iterative two-stage cloud detection scheme, which we call detect and spread (DAS).

Cloud detection is performed on feature domains that are iteratively brought closer to the clear sky origin in feature space. Before the feature domain for the next detection is expanded all the already detected clouds are spread by including pixels that fall in a feature domain that is larger than the one used in the subsequent detection stage. This avoids pixels just outside the edge of already identified clouds being detected as part of a new cloud.

In this particular study, the feature domain consisted of the effective brightness temperatures only. The following four parameters are used to establish the various feature domains (temperature thresholds here):

1. $T_{\min} = 240$ K is the first detection temperature. Consecutive areas with $T < T_{\min}$ are assumed to belong to one cloud (convective systems in our case).
2. $T_{\max} = 285$ K is the maximum T above which new clusters are not identified. Pixels with $T > T_{\max}$ are assumed to be clear.
3. $\Delta T_d = 15$ K; the detection threshold is increased by this value in every new detection stage.
4. $\Delta T_s = 20$ K; the current spreading threshold equals the last detection temperature plus this value.

In short, the detect levels were $T_d(i) = T_{\min} + \Delta T_d$, and the corresponding spread levels were $T_s(i) = T_d(i) + \Delta T_s$ whereby either level was upper bound clipped at $T_{\max} = 285$ K. The spreading in stage i takes place in three iterations with associated levels $T_d(i) + j\Delta T_s/3$, where $j \in \{1, 2, 3\}$. To minimize one cloud being spread around adjacent clouds, new clouds needed to be detected at a T colder than the T to which the existing clouds were spread in the previous step (i.e., $T_d(i + 1) < T_s(i)$, or equivalently, $\Delta T_s > \Delta T_d$). While

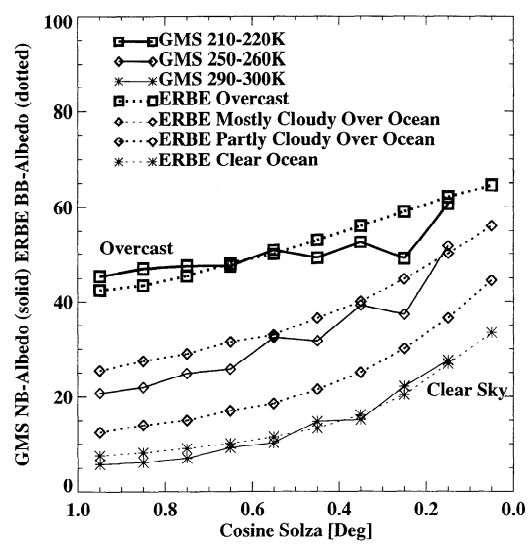

Figure A1. Directional albedo comparison between the ERBE and GMS bidirectional model.

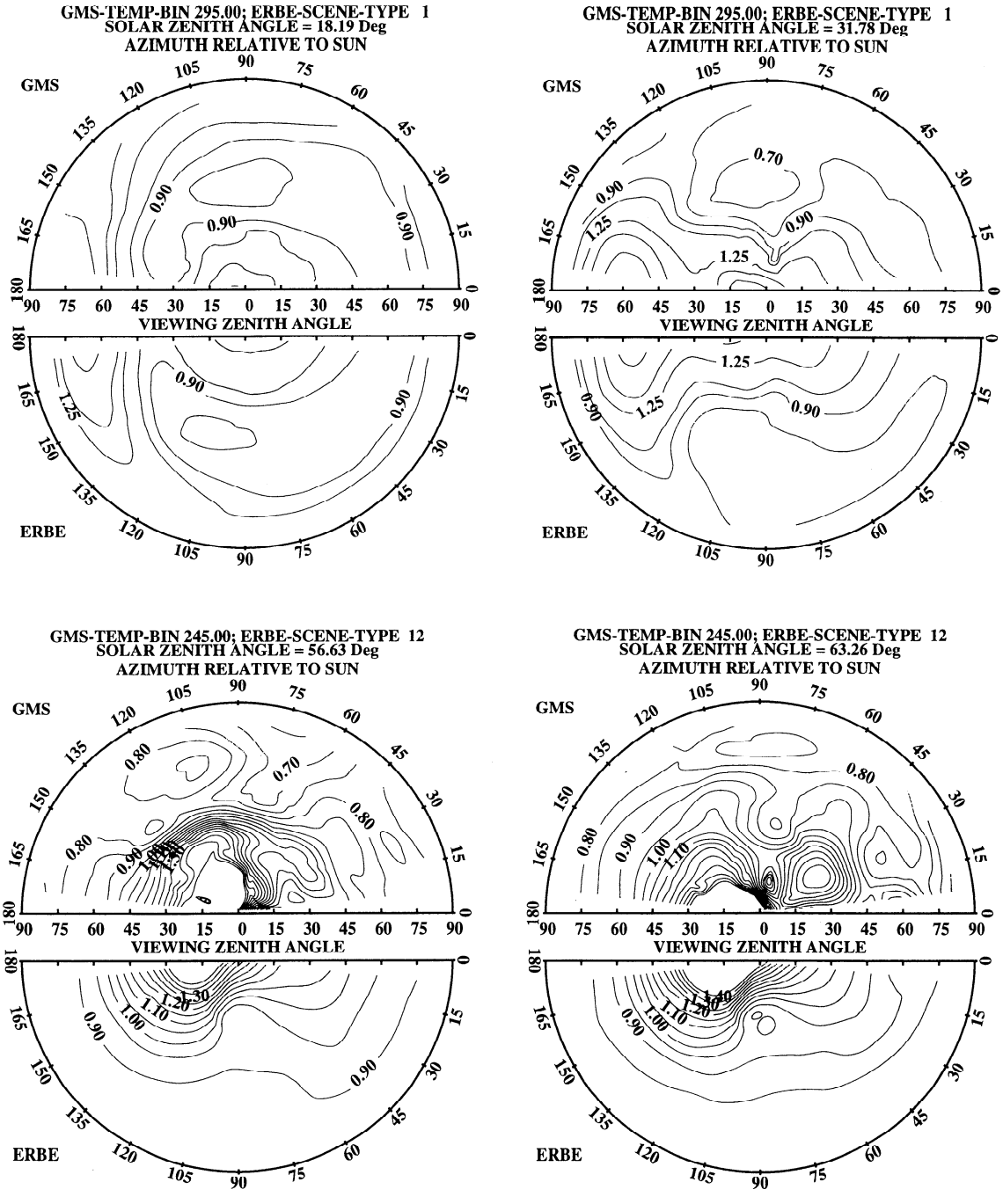

Figure A2. Anisotropic factor comparison between the ERBE and GMS bidirectional model.

$\Delta T_s > \Delta T_d$ could be made to depend on T itself, we decided not to explore the possible advantages.

While no in-depth sensitivity study was performed on the particular choice of $T_{\min}$, $T_{\max}$, ΔT_d, and ΔT_s, insights obtained from a limited sensitivity study are

1. $T_{\max}$ should not be chosen too high since that dramatically reduces the total number of clouds. It should be set to the lowest possible temperature at which one expects individual clouds to be found.

2. Detected clouds should not simply be spread to clear sky ($T_{\min}$) at once since this would cause extremely large clouds in some cases. A hierarchy of constrained detection and spread stages facilitates separation of clouds if they are connected via a local minimum, valley, or saddle point in T.

3. ΔT_s should be based on the expected drop in a cloud's T when moving from its optically thickest area to its edge. We assumed this to be about 20°.

4. $\Delta T_s - \Delta T_d$ as well as ΔT_d should exceed the pixel to pixel variability of a cloud's T as well as the variability or noise introduced by the sensor. In our case, this was assumed to be no more than 5°.

5. In selecting ΔT_d one should simply adhere to the previous two constraints.

The current DAS implementation is very effective when

different clouds are either separated by clear sky or a significant drop in T or similarly when they each have a definitive core. In case of multilevel cloud decks or tightly spaced clouds, DAS causes some clouds to be merged because of the homogeneity in brightness temperatures. Ideally, all the available channel information should be used to establish a feature space in which a cloud's core is preserved as a separate cluster and one where edges of clouds at different altitudes differ greatly. We expect that a marriage of our cloud-object-based view and cloud-clustering techniques such as those described by *Gallaudet and Simpson* [1991] or *Gallegos and Hawkins* [1993] will yield a highly accurate technique for identifying individual clouds. In this case, fewer assumptions or arbitrary choices are needed in establishing the various thresholds of subfeature domains used in DAS. Such improvements are topics of future study.

B.2. Cloud Tracking Algorithm

CTA operates on ellipsoidal equivalents of the MCS identified by DAS. Ellipsoidal representations were used to limit the computational load. To assess the effect of using ellipsoids instead of the true sample distribution, the ratio between the number of pixels outside the ellipsoid and the total number of samples could be calculated. Ellipsoidal equivalents are established as follows. The first step is to compute the center (lon_c, lat_c) and orientation of the set of pixels that form an MCS. The parametric line equations of the major and minor axes were established by minimizing the summed absolute deviation to a straight regression line instead of the square distance because it is known to be more robust [*Press et al.*, 1990, p. 558]. The axis with the smallest spread of points around it was used as the major axis. The orientation or slope angle in the major axis is denoted by θ.

Once the major $\tilde{X}$ and minor $\tilde{Y}$ axes were established, their respective half lengths a and b were calculated on the basis of the standard deviations $\tilde{\sigma}_Y$ and $\tilde{\sigma}_X$ of the points with respect to the major and minor axes. Using standard deviations instead of average distances to the axes assures that points far away from the axes are weighted slightly more, thus better preserving the MCS's aspect ratio. Thus $\tilde{\sigma}_X$ and $\tilde{\sigma}_Y$ are obtained by taking the standard deviation of the distance d of every point (x, y) to the minor and major line equations $y = px + q$, respectively, using [*Strang*, 1980, p. 107]

$$d = \sqrt{\left| \frac{(x^2 + (y - q)^2)(1 + p^2) - (x + p(y - q))^2}{1 + p^2} \right|}$$

One can also compute $\tilde{\sigma}_X$ and $\tilde{\sigma}_Y$ using

$$E\{\tilde{X}\} = E\{X \cos\theta - Y \sin\theta\}$$

$$E\{\tilde{Y}\} = E\{X \sin\theta + Y \cos\theta\}$$

$$\sigma_{\tilde{X}} = \sqrt{\sigma_{X'X} \cos^2\theta + \sigma_{Y'Y} \sin^2\theta - \sigma_{X'Y} \sin\theta \cos\theta}$$

$$\sigma_{\tilde{Y}} = \sqrt{\sigma_{X'X} \sin^2\theta + \sigma_{Y'Y} \cos^2\theta - \sigma_{X'Y} \sin\theta \cos\theta}$$

which are based on a two-dimensional rotational matrix transformation between the longitude/latitude coordinates (X, Y) and the ellipsoid's coordinates $(\tilde{X}, \tilde{Y})$. E represents the expectation operator.

The half lengths a and b are scaled by a factor α to match the area A of the underlying MCS. On the basis of the constraint that $A = ab\pi = \alpha\sigma_{\tilde{X}}\sigma_{\tilde{Y}}$, a and b are obtained from

$$\alpha = \frac{A}{\pi\sigma_{\tilde{X}}\sigma_{\tilde{Y}}}$$

$$a = \sqrt{\alpha}\sigma_{\tilde{X}}$$

$$b = \sqrt{\alpha}\sigma_{\tilde{Y}}$$

A simple least squares based regression on the pixel locations to obtain the major axis produced unsatisfactory overlap between the MCS and its ellipsoidal equivalent. Tests on simulated ellipsoidal clouds showed that such an approach performed best on clouds with large aspect ratios while the slopes of more circular clouds were severely underestimated. The most compelling evidence that this method is inadequate is that least squares regression between longitude and latitude produced very different results from the reverse regression. This discrepancy is due to the fact that least squares looks only at the distance perpendicular to one of the axes and not to the regression line itself as is the case in the algorithm described above.

Two MCS in consecutive time slots M_t and M_{t+1} belong to the same system if either centroid falls inside the ellipsoidal equivalent of the other (overlap). The underlying assumption is that these two MCS are identical if the smallest one has not traveled (forward or backward in time) outside the reach of the other. If multiple MCS at time $t + 1$ fall within the vicinity of M_t, M_t is assumed to have split up, and all these MCS are associated (every MCS across all time steps has a unique numerical label, and association occurs by keeping track of which labels belong to the same system). Similarly, if multiple MCS at t fall in the vicinity of M_{t+1}, then these MCS are assumed to have merged into M_{t+1}. This scheme properly associates merging and splitting systems. To avoid a break in the evolution of an MCS due to bad or missing data, the association process was performed on data from one and two time steps back in time. This approach is similar to the one described by *Williams and Houze* [1987], who track MCS over 3-hour intervals and require 50% overlap between MCS in consecutive time slots instead of our centroid-based ellipsoidal inclusion criterion.

A few words about the tagging system are needed. All MCS in the first time slot t_1 receive a different label. Every MCS in the second time slot t_2 that overlaps with one in t_1 receives that MCS's label. If an MCS in t_2 overlaps with multiple ones in t_1, then they all receive the same label (from one of these MCS in t_1). This relabeling of a set of an MCS in a previous time step (e.g., 7 = 4 = 2) is stored in a table, so that at the end all MCS are relabeled using this information. This assures proper merging. This procedure is repeated for all consecutive time slots.

Acknowledgments. We benefited from numerous discussions with W. D. Collins and J. A. Coakley. We thank R. Bernstein of Sea Space Corp. for providing the GMS data. This work was supported by the Department of Energy ARM grant and by the NSF Science and Technology Center for Clouds, Chemistry and Climate (C^4) grant, and is C^4 publication 151.

References

Baum, B. A., R. F. Arduini, B. A. Wielicki, P. Minnis, and S. Tsay, Multilevel cloud retrieval using multispectral HIRS and AVHRR data: Nighttime oceanic analysis, *J. Geophys. Res.*, *99*, 5499–5514, 1994.

Chen, S. S., and R. A. Houze Jr., Multiscale variability of deep con-

vection in relation to large-scale circulation in TOGA COARE, *J. Atmos. Sci.*, *53*, 1380–1409, 1996.

Coakley, J. A., and F. P. Bretherton, Cloud cover from high resolution scanner data: Detecting and allowing for partially filled fields of view, *J. Geophys. Res.*, *87*, 4917–4932, 1982.

Dlhopolsky, R., and R. D. Cess, Improved angular directional models for clear sky ocean derived from earth radiation budget satellite shortwave radiances, *J. Geophys. Res.*, *98*, 16,713–16,721, 1993.

Gallaudet, T. C., and J. J. Simpson, Automated cloud screening of AVHRR imagery using split-and-merge clustering, *Remote Sens. Environ.*, *38*, 77–121, 1991.

Gallegos, S. C., and J. D. Hawkins, A new automated method of cloud masking for advanced very high resolution radiometer full-resolution data over the ocean, *J. Geophys. Res.*, *98*, 8505–8516, 1993.

Gray, W. M., and R. W. Jacobson Jr., Diurnal variation of deep cumulus convection, *Mon. Weather Rev.*, *105*, 1171–1188, 1977.

Kidwell, K. B., NOAA polar orbitor data users guide (TIROS-N, NOAA-6, NOAA-7, NOAA-8, NOAA-9, NOAA-10, NOAA-11, and NOAA-12), report, Natl. Oceanic and Atmos. Admin., Natl. Environ. Satell., Data and Inf. Serv., Natl. Clim. Data Cent., Satell. Data Serv. Div., Washington, D. C., July 1991.

Kuettner, J. P., Central Equatorial Pacific Experiment: Experiment design, report, Cent. for Clouds, Chem. and Clim., Scripps Inst. of Oceanogr., Univ. of Calif., San Diego, 1993.

Kwok, R., J. C. Curlander, R. McConnell, and S. S. Pang, An ice-motion tracking system at the Alaska SAR facility, *IEEE J. Oceanic Eng.*, *15*, 44–54, 1990.

Laing, A. G., and M. Fritsch, Mesoscale convective complexes over the Indian monsoon region, *J. Clim.*, *6*, 911–919, 1993.

Leary, C. A., and R. A. Houze, The structure and evolution of convection in a tropical cloud cluster, *J. Atmos. Sci.*, *36*, 437–457, 1979.

Lee, J., J. Chou, R. C. Weger, and R. M. Welch, Clustering, randomness, and regularity in cloud fields, 4, Stratocumulus cloud fields, *J. Geophys. Res.*, *99*, 14,461–14,480, 1994.

Lin, A., and J. A. Coakley Jr., Retrieval of properties for semitransparent clouds from multispectral infrared imagery data, *J. Geophys. Res.*, *98*, 18,501–18,514, 1993.

Liu, G., J. A. Curry, and R. S. Sheu, Classification of clouds over the western equatorial Pacific Ocean using combined infrared and microwave satellite data, *J. Geophys. Res.*, *100*, 13,811–13,826, 1995.

Lopez, R. E., The lognormal distribution and cumulus cloud populations, *Mon. Weather Rev.*, *105*, 865–872, 1977.

Machado, L. A. T., M. Desbois, and J.-P. Duvel, Structural characteristics of deep convective systems over tropical Africa and the Atlantic Ocean, *Mon. Weather Rev.*, *120*, 392–406, 1992.

Machado, L. A. T., J.-P. Duvel, and M. Desbois, Diurnal variations and modulations by easterly waves of the size distribution of convective cloud clusters over west Africa and the Atlantic Ocean, *Mon. Weather Rev.*, *121*, 37–49, 1993.

Mapes, B. E., Gregarious tropical convection, *J. Atmos. Sci.*, *50*, 2026–2037, 1993.

Mapes, B. E., and R. A. Houze Jr., Cloud clusters and superclusters over the oceanic warm pool, *Mon. Weather Rev.*, *121*, 1398–1415, 1993.

Nakazawa, B. T., Tropical super clusters within intraseasonal variations, *J. Meteorol. Soc. Jpn.*, *66*, 823–839, 1988.

Press, W. H., B. P. Flannery, S. A. Teukolsky, and W. T. Vetterling, *Numerical Recipes in C*, Cambridge Univ., New York, 1990.

Senta, K. E., *The GMS Users' Guide*, 2nd ed., Meteorol. Satell. Cent., Tokyo, Japan, 1989.

Strang, G., *Linear Algebra and Its Applications*, 2nd ed., Academic, San Diego, Calif., 1980.

Stuhlmann, R., P. Minnis, and G. L. Smith, Cloud bidirectional reflectance functions: A comparison of experimental and theoretical results, *Appl. Opt.*, *24*, 396–401, 1985.

Sundqvist, H., Parameterization scheme for nonconvective condensation, including prediction of cloud water content, *Q. J. R. Meteorol. Soc.*, *104*, 677–690, 1978.

Suttles, J. T., NASA/ASD, generation of shortwave bi-directional and albedo models for analysis of Earth radiation budget data, *Tech. Rep. 3-92000/6TR-561*, Plann. Res. Corp., Kentron, Aerospace Technologies Division, Hampton, Va., 1986.

Wielicki, B. A., and L. Parker, On the determination of cloud cover from satellite sensors: The effect of sensor spatial resolution, *J. Geophys. Res.*, *97*, 12,799–12,823, 1992.

Williams, M., and R. A. Houze Jr., Satellite-observed characteristics of winter monsoon cloud clusters, *Mon. Weather Rev.*, *115*, 505–519, 1987.

Williams, S. F., Central Equatorial Pacific Experiment: Operations Summary, report, Univ. Corp. of Atmos. Res., Off. of Field Proj. Support, Boulder, Colo., 1993.

Xianjin, F., Spectral and anistropic corrections for GMS satellite data, *Adv. Atmos. Sci.*, *9*, 287–298, 1992.

E. R. Boer, Nissan Cambridge Basic Research, 4 Cambridge Center, Cambridge, MA 02142.

V. Ramanathan, Center for Atmospheric Sciences, Center for Clouds, Chemistry and Climate, Scripps Institution of Oceanography, University of California at San Diego, La Jolla, CA 92093. (vramanathan@ucsd.edu)

(Received November 22, 1995; revised January 24, 1997; accepted February 25, 1997.)